



Localized heat transfer from firebrands to surfaces

Elias D. Bearinger^a, Jonathan L. Hodges^b, Fengchang Yang^b, Christian M. Rippe^b,
Brian Y. Lattimer^{a,*}

^a Virginia Tech, Mechanical Engineering, 635 Prices Fork Rd, Blacksburg, VA, USA

^b Jensen Hughes, 2020 Kraft Dr, Suite 3020, Blacksburg, VA, USA

ARTICLE INFO

Keywords:
Firebrand
Heat transfer
Surface
Ignition

ABSTRACT

Firebrands are known to cause spot fires and structure ignition far from the fire front, but there is a limited understanding of the heat transfer from firebrands to surfaces. In this work, high resolution heat flux distributions were measured for single firebrands with different geometries using IR thermography and inverse heat transfer analysis. Localized heat fluxes from a single firebrand were measured to be 30–105 kW/m², which is 2–6 times higher than previous work with heat flux gauges and energy balance methods that spatially average the heat transfer from the firebrand. Firebrand geometry, wind speed, and wind speed orientation relative to the firebrand affect the heat flux magnitude and duration of the exposure.

1. Introduction

Wildland fires continue to threaten urban communities due to overgrown vegetation and the increasing number of structures built in the wildland area. In these wildland fires, firebrands are lofted far from the fire front where they ignite vegetation and structures starting spot fires. Due to the uncertainty of where firebrands will land, these spot fires can result in significant damage due to not being detected until flames have started to spread across the vegetation or structure. As a result, significant research has focused on understanding the generation, transport, and ignition processes due to firebrands as described in several reviews [1–4]. One area cited in these reviews as needing more attention is a better fundamental understanding of how firebrands ignite combustible materials and vegetation. This requires quantifying conditions for firebrands to ignite fuels, firebrand temperature, and heat transfer from the firebrand to the surface.

Early work to understand the ignition of combustible materials and vegetation by firebrands focused on determining the amount of firebrands required to cause different fuels to ignite. Dowling [5] investigated the required amount firebrands to ignite wood bridges and determined that firebrand piles of at least 7g of firebrands produced from wood cribs was needed to cause smoldering ignition. The size and shape of the firebrands was not quantified. Ellis [6] conducted experiments with Jarrah messmate stringybark (50 mm long, 15 mm, 5 mm weighing 0.7–1.8g) and determined that flaming firebrands could cause

flaming ignition of pine needles with a moisture content (MC) less than 8%. Flaming ignition of pine needles by glowing firebrands was dependent on the presence of wind and the MC of the pine needles. With no wind, glowing firebrands would only cause the pine needles to smolder. In the presence of wind, the probability of flaming ignition increased with a decrease in MC (10–20% probability with a MC = 8% to over 50% probability with a MC < 6%). This result is similar to that found by Ohlemiller [7] in wood smoldering experiments, where the presence of wind was necessary to cause a transition from smoldering ignition to flaming ignition.

Manzello et al. [8] conducted experiments to quantify ignition of fuel beds of pine needles, shredded paper, and hardwood mulch with single and multiple firebrands. Fuel beds were tested dry and with a MC = 11% under wind conditions of 0.5 and 1.0 m/s. Ponderosa pine firebrands were cylindrical in shape (5 mm diameter, 51 mm long, 0.2g mass and 10 mm diameter, 76 mm long, 0.67g mass) to represent those generated from Douglas fir tree fires. Flaming firebrands caused flaming ignition in all cases except hardwood mulch at a MC = 11%. A single glowing firebrand (5 mm and 10 mm diameter) caused smoldering ignition of dry and MC = 11% shredded paper, but no ignition was observed for pine needles or hardwood mulch. Pine needles required four 10 mm diameter firebrands (2.68 g) with 1.0 m/s wind for smoldering ignition, which transitioned to flaming. In a separate study, Manzello et al. [9] investigated the ignition of pine needles and shredded paper by Ponderosa pine firebrand disks (25 mm and 50 mm diameter with a 8 mm

* Corresponding author.

E-mail address: lattimer@vt.edu (B.Y. Lattimer).

<https://doi.org/10.1016/j.firesaf.2020.103037>

Received 14 January 2020; Accepted 28 April 2020

Available online 4 May 2020

0379-7112/© 2020 Elsevier Ltd. All rights reserved.

thickness). Compared with the cylinders, a larger mass of firebrand disks were required to cause ignition of the fuel beds. This was attributed in part due to the contact between the fuel bed and the firebrand, including the cylindrical firebrands falling into the fuel bed. Simulations on the effect of contact resistance between firebrands and a wood surface has also shown that decreasing contact resistance increases the temperature rise of wood [10].

Manzello et al. [11] tested the potential for piles of 10 mm diameter, 76 mm long Ponderosa pine glowing firebrands to ignite oriented strand board (OSB) and plywood butted together at different angles (60–135°). Piles contained 2–4 firebrands placed in the crevice of the angled boards with wind ranging from 1.3 to 2.4 m/s. With dried boards, at least 3 glowing firebrands (2.01 g) were required to cause smoldering ignition with the angle at 60° and 4 glowing firebrands (2.68 g) with the boards at 90°. Hakes et al. [12] placed a pile of 12 mm diameter birch firebrands (9.6 g) onto a horizontal OSB board and observed sustained ignition after 90 s. In experiments with a firebrand shower onto different types of wood decks, the mass of firebrands applied onto the deck for ignition varied from 89 to 283 g with the required mass dependent on the type of wood [13]. Experiments were also conducted on home insulations [14] using a 10 mm diameter, 50 mm long cylindrical firebrand (0.4 g) or four 10 mm diameter, 10 mm long firebrands (0.4 g). Fibrous combustible materials (denim, cellulose) were observed to ignite from a single firebrand. Applying the pile of 4 firebrands with the same mass and increasing the wind speed caused the ignition time to decrease. Comparing ignition times from the firebrand tests to those in the cone calorimeter, the heat flux from the firebrand to the material was approximately 35 kW/m². The synthetic insulation boards (polyurethane, polystyrene) did not ignite in part due to the firebrand softening the material and sinking down into the insulation. These studies indicate that the likelihood of ignition increases with an increase in the firebrand pile size, fuel type, and geometry of the fuel surface. Also, they highlight the complexity of the heat transfer between the firebrands and the fuel surfaces resulting in a ranging of ignition conditions.

An important part of quantifying the exposure is measuring the temperature of the firebrand. Optical techniques have been used by researchers to quantify the firebrand temperature. Color pyrometry and infrared (IR) thermography were used to quantify temperatures of firebrands 6.5–15.9 mm in diameter at wind speeds of 1–4 m/s [15]. Average temperatures ranged from 750 to 875 °C at 1 m/s to 800–950 °C at 4 m/s. Manzello et al. [11] measured average surface temperatures of 550–600 °C with 1.3 m/s of wind and 680–700 °C for 2.4 m/s of wind. In experiments by Wessies et al. [14], firebrand temperatures were 783 °C for 2.0 m/s wind and 824 °C with 9 m/s of wind. All studies confirm that increasing the wind speed increases the firebrand temperature due to more surface char oxidation. Some of the temperature variation between studies may be due to the surface emissivity of the firebrand used in the measurement. Emissivity values for firebrands were determined to range from 0.6 to 0.8 [11,14,15] resulting in an average value of 0.7.

Limited measurements have been conducted on the heat transfer from the firebrand to a surface. Manzello et al. [11] used an energy balance and the firebrand temperature to estimate the average heat transfer across the firebrand to the surface. For a single glowing cylindrical firebrand, the average heat flux over the firebrand was predicted to be 23 kW/m² with 1.3 m/s of wind and 34 kW/m² with 2.4 m/s of wind. Water cooled heat flux gauges and thin skin calorimeters with 12 mm diameter sensing surfaces were used to measure heat flux levels from single and piles of firebrands [12]. For single cylindrical firebrands (6.35–12.7 mm diameter, 25.4 mm long, 0.1–0.6 g mass), the heat fluxes were measured to be 7–25 kW/m² with no wind. Since the sensor gauge is similar to the size of the firebrand, these heat fluxes represent an average heat flux from the firebrand and are in good agreement with those predicted by Manzello et al. [11] through an energy balance. However, the heat fluxes are lower than expected based on some of the local firebrand surface temperatures.

The focus of this paper is to provide high resolution measurements of

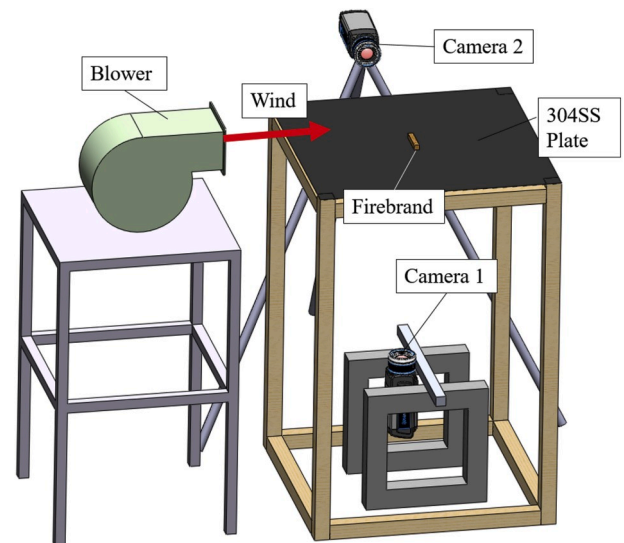


Fig. 1. Test stand to characterize localized heat transfer from firebrands.

the heat transfer from a firebrand to a horizontal surface to capture the spatial variation below and around the firebrand. Ignition is a local phenomenon that will depend on the highest heat transfer levels from the firebrand. Since the contact between the firebrand and surface may be variable and the air flow around the firebrand may change its temperature non-uniformly, spatial distributions in the heat transfer from the firebrand to the surface are needed to quantify the highest heat transfer levels to assess ignition potential. Recently, a technique using a Nd:YAG laser based method was developed with a patterned quartz platform and a CMOS camera to quantify heat flux at higher resolutions; however, no measurements have been conducted on firebrands to date [16]. In this work, the inverse heat transfer method using IR thermography of a stainless steel plate [17,18] was used to quantify high resolution heat flux distributions from a single firebrand placed on a horizontal surface. The effects of firebrand geometry, firebrand contact with the surface, wind speed, and firebrand orientation with the wind on the heat flux to the surface were quantified. Localized heat flux measurements were spatially averaged to compare with other measurements in the literature.

2. Experimental methods

A series of experiments were performed to quantify the spatial and temporal variation in heat flux from a single firebrand to a surface. An inverse heat transfer method using IR thermographs was used to quantify the heat flux from the firebrand to the surface at a resolution of 0.4 mm. A description of the apparatus, firebrands, and inverse heat transfer method is provided below along with the test matrix performed in this study.

2.1. Test apparatus

The experimental setup to quantify the heat transfer from a single firebrand to a surface is shown in Fig. 1. The setup consisted of a thin 304SS stainless steel plate painted black, an IR camera to measure temperature of the underside of the plate (Camera 1), an IR camera to measure the firebrand temperature (Camera 2), and a blower to provide wind. Firebrands were placed on a 0.8 mm thick 304SS plate painted black on both sides with four coats of Rust-Oleum™ high-heat black paint with a measured emissivity of $\epsilon = 0.97$ [19]. The stainless steel plate was square with each side being 0.61 m long and was supported in each corner by a wooden stand. The wooden stand was 0.92 m tall and sufficiently stable that the plate did not move during the testing.

Two FLIR A655sc infrared cameras operating in the 7–14 μm wavelength range were used to measure surface temperatures. The cameras had a 640×480 pixel resolution and used a 24.6 mm (25°) lens. Camera 1 was used to measure the underside of the steel plate and was operated in the $-40 - 150^\circ\text{C}$ or $100 - 650^\circ\text{C}$ calibration range, depending on the test conditions. Camera 1 was 0.58 m below the underside of the steel plate resulting in a field of view of the plate of 0.259 m by 0.195 m, which corresponds to a spatial resolution of 0.4 mm. The emissivity for Camera 1 was set to 0.97 to correspond to the black paint emissivity. Camera 2 measured the firebrand surface temperature and was operated using the $100 - 650^\circ\text{C}$ or $300 - 2000^\circ\text{C}$ calibration range, depending on the test conditions. The distance between Camera 2 and the firebrand ranged from 0.40 to 0.50 m resulting in a spatial resolution of 0.28–0.35 mm of temperature on the firebrand. Camera 2 emissivity was set to a value of $\varepsilon = 0.7$ which is the average of the range of emissivity levels (0.6–0.8) reported in the literature for firebrands [11,14,15]. ResearchIR software was used to control the cameras, collect data, and produce thermal images.

Wind was provided by a Dayton Model No. 1TDR3 Blower (273 cfm @ free air and 60 Hz), connected to a Staco Energy Products Model 3PN151OB Variable Autotransformer to control the wind speed between 0.5 and 2.0 m/s at the firebrand location. The blower was set up such that bottom of the blower outlet was flush with the top of the plate and the flow traveled parallel to the surface. The bottom of the plate was shielded from the airflow so that there was only natural convection below the plate. Wind speed was verified prior to each test using an Extech Hot Wire Thermo-Anemometer with a 0.2–20 m/s range and 0.1 m/s resolution.

2.2. Heat transfer measurement

The thermal exposure from firebrands to adjacent surfaces was measured using the inverse heat transfer technique developed by Rippe et al. [18]. The technique involves painting a stainless steel plate with a known emissivity paint and exposing one side of the plate to the thermal environment. A series of high resolution IR thermography images of the non-exposed side of the stainless steel plate are recorded during testing. An energy balance on each pixel in the IR thermograph is used to calculate the exposure heat flux at every point on the surface using

$$q''_{exp} + q''_{cond} + q''_{rad,b} + q''_{conv,b} = \frac{\rho V c_p}{A} \frac{dT_s}{dt} \quad (1)$$

where q''_{exp} is the exposure heat flux, q''_{cond} is the net lateral heat flux entering a pixel from its neighbors, $q''_{rad,b}$ is the net radiation flux into the non-exposed surface, $q''_{conv,b}$ is the net convection flux into the non-exposed surface, ρ is the density of the stainless-steel plate, V is the volume of the pixel, A is the surface area of the pixel, c_p is the specific heat of the stainless steel plate, and dT_s/dt is the time rate of change of the surface temperature of the pixel. The exposure flux can be expressed as a standard heat flux (typically measured with a Schmidt-Boelter gauge) using the equation

$$q''_0 = q''_{exp} - \varepsilon_f \sigma (T_s^4 - T_0^4) - h_f (T_s - T_0) \quad (2)$$

where q''_0 is the standard heat flux, ε_f is the emissivity of the exposed surface, h_f is the convective heat transfer coefficient on the exposed surface, T_s is the measured surface temperature of the stainless steel plate, and T_0 is the standard temperature taken to be 293 K.

Rippe et al. showed the uncertainty in the thermal exposure measurements decreased with a larger Δt used in the calculation of the energy storage term in Eq. (1). In this work, Δt of 3 s was used in Eq. (1).

The Nusselt number for natural convection of the heated plate was calculated using the relationships presented by Ref. [20,21]. For the upper surface of the heated plate,

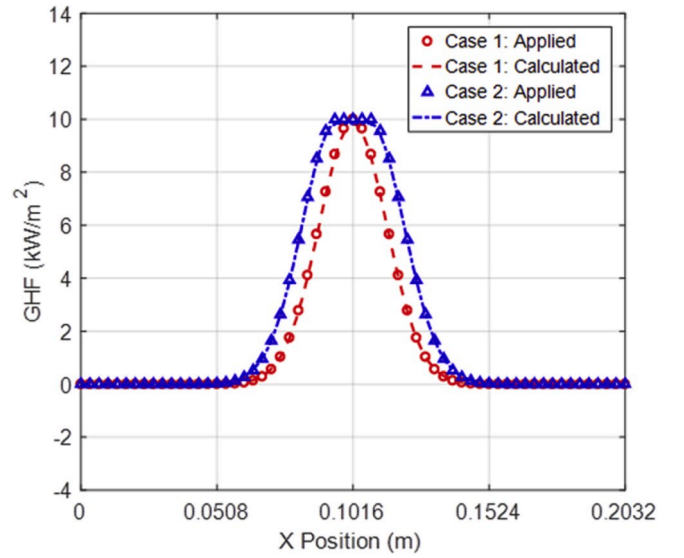


Fig. 2. Verification for quantifying localized heat transfer using the IHT measurement.

$$\overline{Nu}_L = 0.54 Ra_L^{1/4} \text{ for } (10^4 \leq Ra_L \leq 10^7), \quad (3)$$

$$\overline{Nu}_L = 0.15 Ra_L^{1/4} \text{ for } (10^7 \leq Ra_L \leq 10^{11}) \quad (4)$$

where \overline{Nu}_L is the average Nusslet number, and Ra is the Rayleigh number,

$$Ra_L = \frac{g\beta(T_s - T_\infty)L^3}{\nu\alpha} \quad (5)$$

where g is the acceleration due to gravity, β is the thermal expansion coefficient, T_∞ is the ambient air temperature, ν is the kinematic viscosity, α is the thermal diffusivity, and L is the hydraulic radius of the heated section

$$L = \frac{A_{exp}}{P_{exp}} \quad (6)$$

where A_{exp} is the total area exposed by the firebrand, and P_{exp} is the total perimeter exposed by the firebrand. Similarly, \overline{Nu}_L for the lower surface of the heated plate,

$$\overline{Nu}_L = 0.27 Ra_L^{1/4} \text{ for } (10^5 \leq Ra_L \leq 10^{10}). \quad (7)$$

The Nusselt number for forced convection of the heated plate was calculated using the relationships presented by Ref. [22] for fully turbulent boundary layer conditions over a heated flat plate,

$$\overline{Nu}_L = 0.037 Re_w^{4/5} Pr^{1/3} \text{ for } (Re_w \leq 10^8, 0.6 \leq Pr \leq 60) \quad (8)$$

where Re_w is the Reynolds number defined by the plate width, W , and Pr is the Prandtl number.

During preliminary testing, it was observed that the Wiener filter recommended by Rippe et al. to reduce the noise in the thermographs prior to the inverse heat transfer calculation resulted in an increase in noise in this application. In this work, the filter was replaced with a 2-D Gaussian filter with a 7×7 pixel window. The updated filtering approach reduced the peak measured temperature by approximately 1°C , and reduced the peak observed heat flux by 10%.

This series of tests were the first to use the inverse heat transfer (IHT) software in a situation where the thermal response of the stainless steel plate was highly dependent on the spatially resolved conductive flux. Verification of the inverse heat transfer (IHT) software is provided in

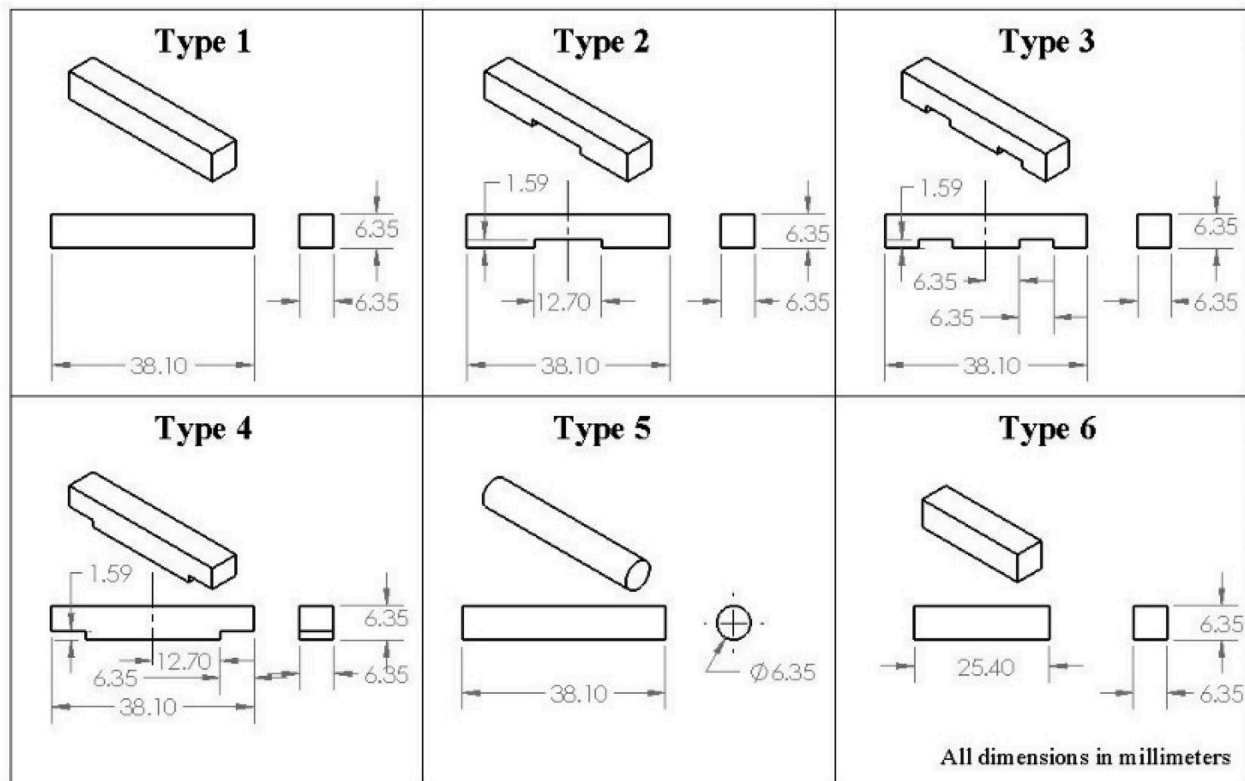


Fig. 3. Oak firebrand geometries.

Fig. 2 for a local exposure on a steel plate similar to what would occur in the firebrand testing.

The IHT software was tested by generating artificial thermographs using known exposure profiles in a Finite Element (FE) model in Abaqus. The model included a 0.20 m by 0.18 m plate with continuum heat transfer elements (DC3D8) at a mesh of density of 0.4 mm/element, which was similar to the spatial resolution of the experimental measurements. As seen in Fig. 2, two verification scenarios were considered with a local heat flux applied to the center of the plate. Verification Case 1 applied a Gaussian distributed heat flux with a peak value of 10 kW/m² applied at the center with $\sigma = 0.0127$ m in shorter dimension and $\sigma = 0.0254$ m in the longer dimension. Verification Case 2 used the uniform 10 kW/m² heat flux over a 0.025 m × 0.051 m wide rectangle with a Gaussian drop at each edge of the uniform region using the same parameters as verification Case 1. The error was less than 1%.

2.3. Firebrands

Firebrands were fabricated using oak wood. Six distinct firebrand geometries were manufactured as shown in Fig. 3. All firebrands had the same aspect ratio and projected area with the exception of Type 6.

Types 1–4 were all cuboids of the same major dimensions (6.35 mm × 6.35 mm, 38.1 mm long) but with different notches on the face that would be in contact with steel plate surface. The notch depth was 1.59 mm in all cases and spanned the entire width of the firebrand. Type 5 was a cylindrical firebrand (6.35 mm diameter, 38.1 mm long) while Type 6 was a cuboid with no notch and a shorter length (6.35 mm × 6.35 mm, 25.4 mm long). The cuboid firebrands were manufactured by using a band saw to cut a 38.1 mm × 6.35 mm board into 6.35 mm strips. Notches were installed by hand, using a Dremel rotary cutter. Type 5 firebrands were manufactured by cutting a 6.35 mm round oak dowel into 38.1 mm sections.

Prior to ignition, each firebrand was weighed using a Sartorius FB6CCE-S scale with a 6200 g range and 0.1 g resolution. To ignite the

Table 1
Firebrand test matrix.

Firebrand Geometry	Description	Wind (m/s)	Wind Orientation	Wood Initial Mass (g)	Firebrand Mass After 300s (g)
Type 1	Cuboid – 6.4 mm × 6.4 mm, 38 mm long	None	N/A	1.1	0.5
		1.0	Parallel	1.2	0.4
		1.0	Perpendicular	1.1	0.1
Type 2	Cuboid – 6.4 mm × 6.4 mm, 38 mm long	None	N/A	1.1	0.3
		1.0	Parallel	1.1	0.3
		0.5	Perpendicular	1.1	0.3
		1.0	Perpendicular	1.1	0.0
		1.5	Perpendicular	1.2	0.0
Type 3	Cuboid – 6.4 mm × 6.4 mm, 38 mm long	None	N/A	1.1	0.3
		1.0	Parallel	1.1	0.1
		1.0	Perpendicular	1.1	0.0
		2.1	Perpendicular	1.1	0.0
Type 4	Cuboid – 6.4 mm × 6.4 mm, 38 mm long	None	N/A	1.1	0.3
		1.0	Parallel	1.1	0.3
		1.0	Perpendicular	1.1	0.3
Type 5	Cylinder – 6.4 mm diameter, 38 mm long	None	N/A	1.1	0.5
		1.0	Parallel	1.1	0.3
		1.0	Perpendicular	1.1	0.5
Type 6	Cuboid – 6.4 mm × 6.4 mm, 25 mm long	None	N/A	0.8	0.2
		1.0	Parallel	0.8	0.0
		1.0	Perpendicular	0.7	0.1

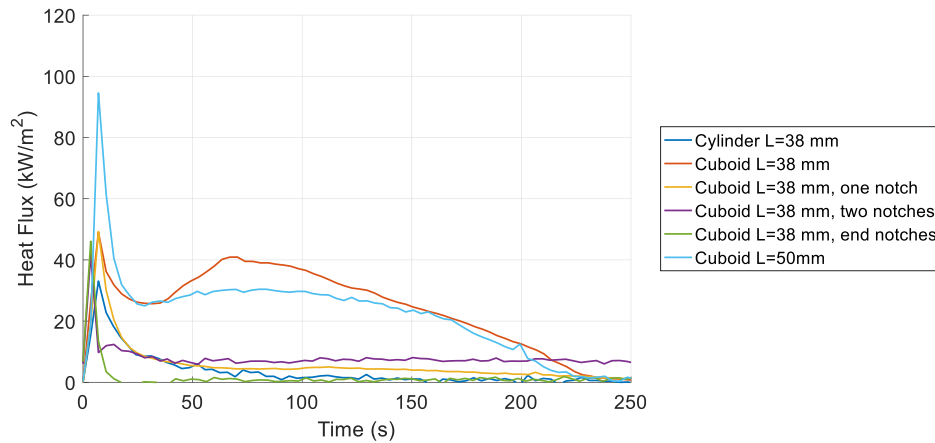


Fig. 4. Heat flux at the peak location with time for different types of firebrands with no wind.

firebrands, a small propane burner was used. The firebrands were placed in a wire mesh basket over the flames, and rotated frequently to ensure even heating on all sides. Heating over the propane flame lasted for 30 s for all firebrands. After the 30 s heating period, the flame was turned off and the firebrand was allowed to progress in a state of flaming ignition for an additional 10 s before the flame was blown out. The glowing firebrand was then placed in the center of the stainless steel plate using tongs for testing.

2.4. Test procedure and matrix

A matrix of experiments was designed to characterize the effect of wind and wind orientation on the heat transfer from the different types of firebrands. Each firebrand geometry (Types 1–6) was tested under three conditions as outlined in Table 1. This included a no wind condition, wind direction that was parallel to the long-axis of the firebrand, and wind direction perpendicular to the long-axis of the firebrand.

The majority of testing was performed with a wind speed was 1.0 m/s, with the exception of the Type 2 firebrands (cuboid with one centered notch) oriented perpendicular to the wind where the wind speed was varied from 0 to 2.0 m/s. For all tests, the firebrands were left on the plate for 300 s. The initial mass of the wood before creating the firebrand

is provided in Table 1 along with the firebrand mass after the 300 s test. The initial firebrand mass before it was put on the plate was approximately 50–60% of the wood initial mass. Results presented in this paper are based on a single firebrand test for each test condition in the matrix provided in Table 1.

3. Results

Heat transfer measurements from the different types of firebrands are presented in this section for different wind conditions and firebrand orientations relative to the wind direction. In addition, temperature measurements on the long side of the firebrand are provided.

3.1. No wind

The heat flux with time at the location on the firebrand where the peak occurs during the test is provided in Fig. 4 for the different types of firebrands tested with no wind. The peak heat flux for all firebrands occurred in the initial 25 s and then the heat flux decayed with time. Peaks were measured to range from 30 to 90 kW/m² with shorter cuboid (L = 25 mm) producing the highest heat flux. The cuboids without notches were measured to have the highest heat fluxes with time while

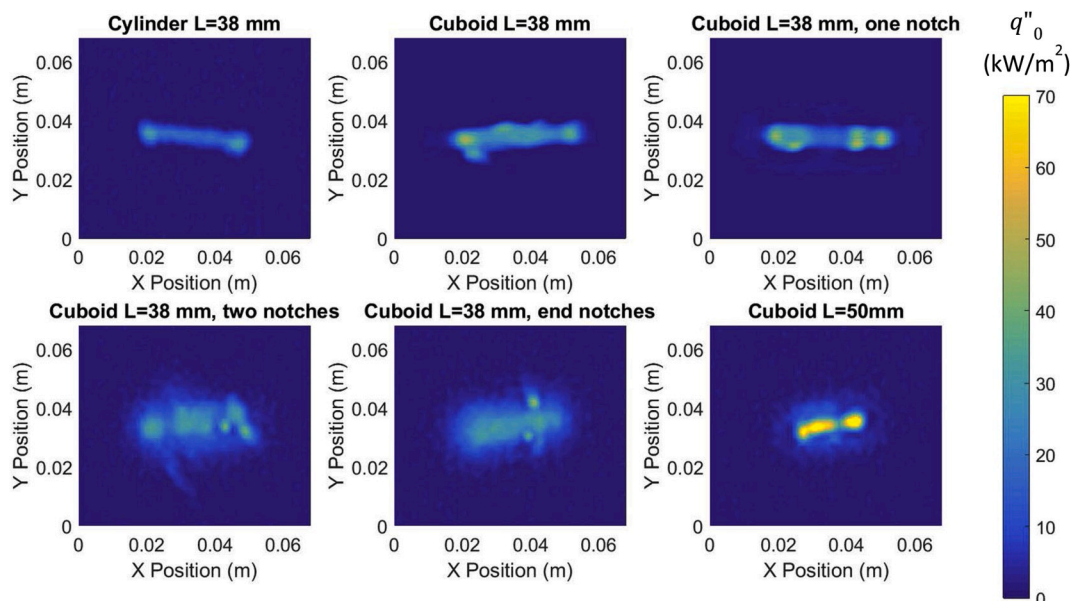


Fig. 5. Heat flux distributions at time of peak for different types of firebrands with no wind.

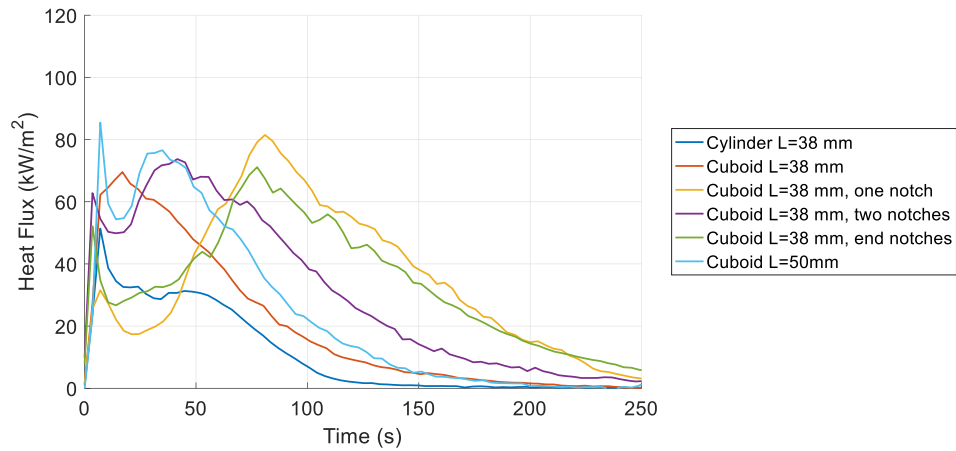


Fig. 6. Heat flux at the peak location with time for different types of firebrands with long side parallel to 1.0 m/s of wind.

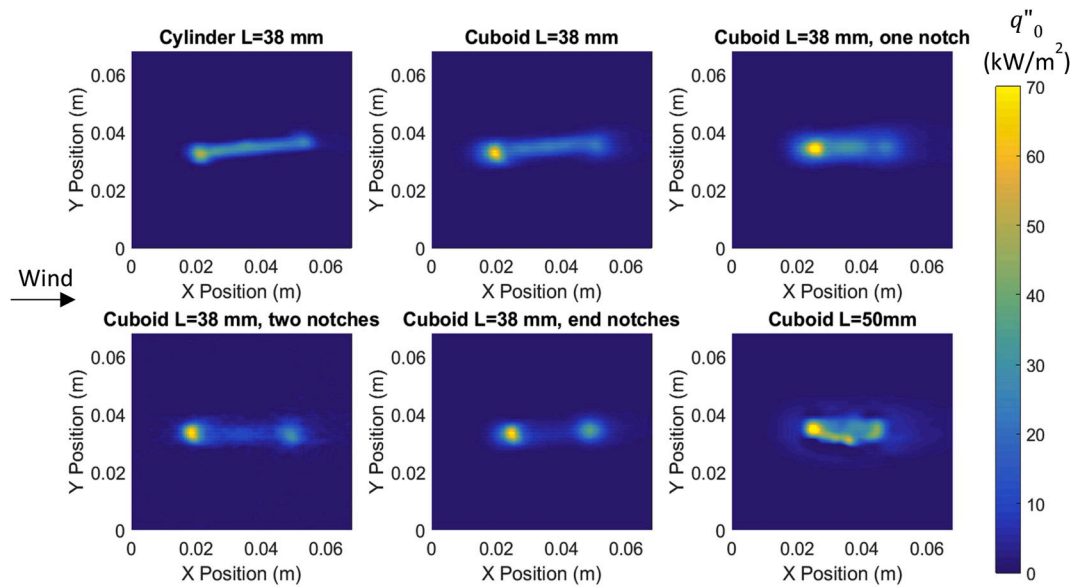


Fig. 7. Heat flux distributions at time of peak for different types of firebrands with long side parallel to 1.0 m/s of wind.

adding notches to the bottom of the firebrand resulted in lower peaks and a more rapid decay in heat flux. The cylindrical fire brand was measured to peak and decay rapidly similar to the cuboids with notches. The spatial distribution in the heat flux at the time of the peak is

provided in Fig. 5. Except for the cuboid with one notch, the heat flux is relatively uniform beneath the firebrands.

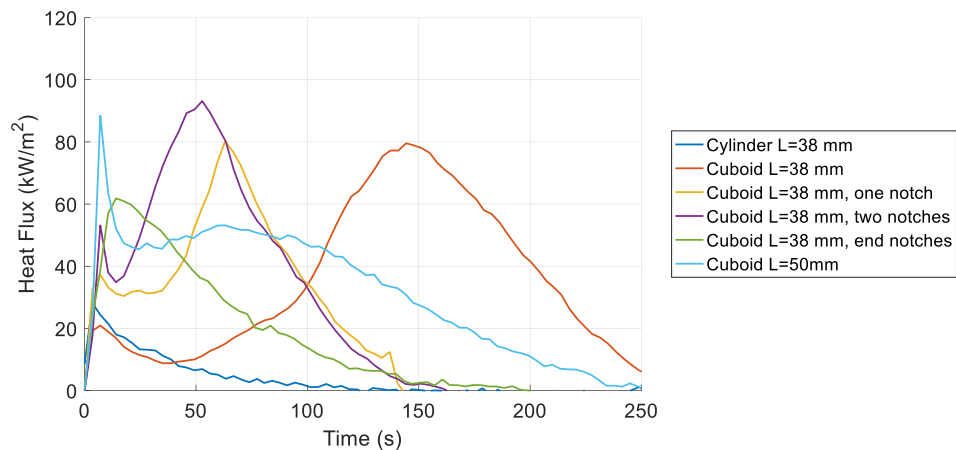


Fig. 8. Heat flux at the peak location with time for different types of firebrands with long side perpendicular to 1.0 m/s of wind.

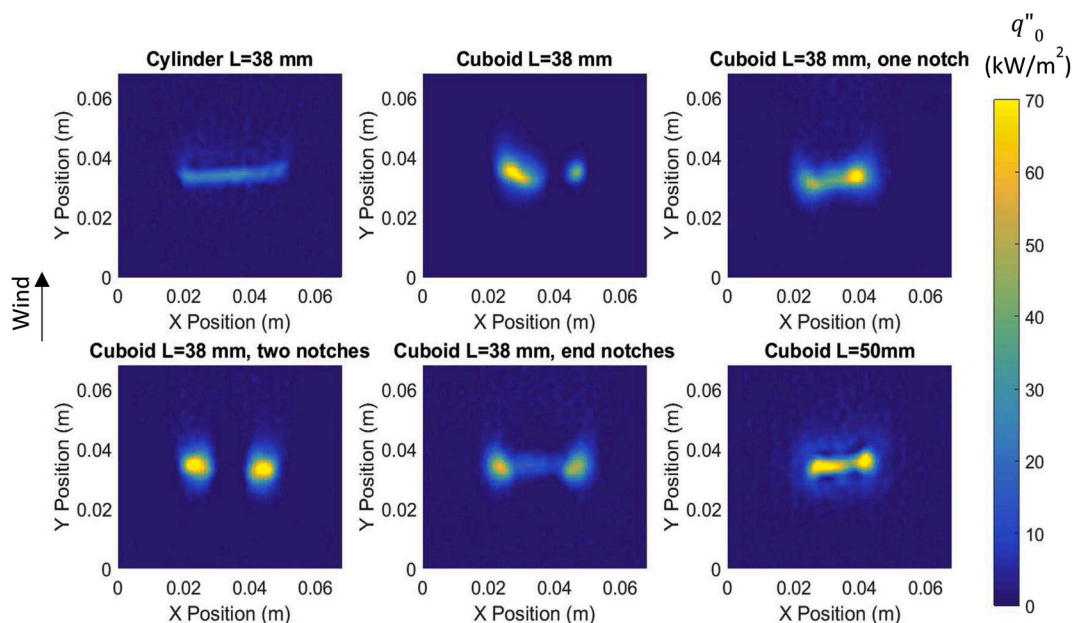


Fig. 9. Heat flux distributions at time of peak for different types of firebrands with long side perpendicular to 1.0 m/s of wind.

3.2. Parallel wind

The heat flux with time at the location on the firebrand where the peak occurs during the test is provided in Fig. 6 for the different types of firebrands tested with the long side parallel to 1.0 m/s of wind. Compared with the no wind case in Fig. 4, these heat fluxes are generally higher and remain at an elevated level for a longer period of time. Peak heat fluxes ranged from 55 to 85 kW/m². For this case, the firebrand exposure remains above 20 kW/m² for 75–185 s, depending on the type of firebrand, and had a characteristic double peak in the heat flux before decaying. The cylindrical firebrand produced the lowest heat fluxes and had the shortest duration. The highest heat fluxes were measured to be the shorter cuboid ($L = 25$ mm) and the cuboid with a single notch. In comparing the cuboid $L = 38$ mm (flat) with cuboids with notches, the firebrands with notches tend to have lower heat fluxes in the initial 25–50 s of exposure, but then increase above the flat firebrand at longer times.

The spatial distribution in heat flux from the firebrands are provided in Fig. 7 at the time of the peak heat flux. For this case, the highest heat

fluxes are generally at the leading edge of the firebrand where the wind initially encounters the firebrand. The notches in the firebrands are not where the highest heat fluxes are measured, except in the case with the end notches where the leading edge is at the notch location.

3.3. Perpendicular wind

The heat flux with time at the location on the firebrand where the peak occurs during the test is provided in Fig. 8 for the different types of firebrands tested with the long side perpendicular to 1.0 m/s of wind. In this case, a double peak heat flux exposure is measured with peak heat fluxes of 30–90 kW/m². Exposure of greater than 20 kW/m² ranged from 10 to 175 s. The cylindrical firebrand produced the lowest heat flux while the shorter cuboid ($L = 25$ mm) generated the highest heat fluxes. Adding notches to the cuboids ($L = 38$ mm) resulted in higher heat fluxes within the initial 100 s; however, the flat cuboid ($L = 38$ mm) heat flux increased later in the experiment peaking at 80 kW/m². In general, these firebrand exposures were similar in magnitude and duration compared with the parallel wind case (Fig. 6); however, the individual

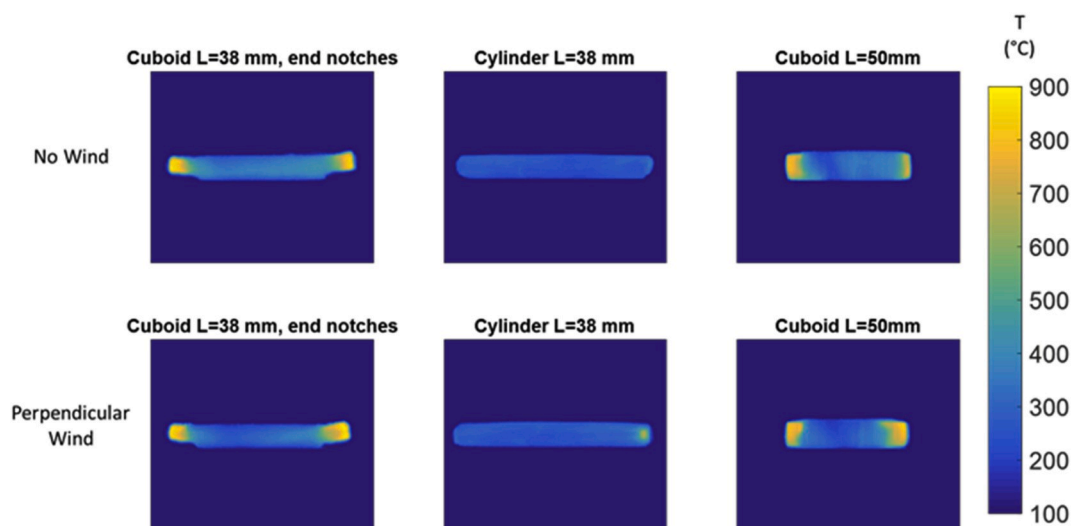


Fig. 10. Firebrand temperature distribution at the time of peak temperature for no wind (top row) and firebrand perpendicular to wind at 1.0 m/s (bottom row).

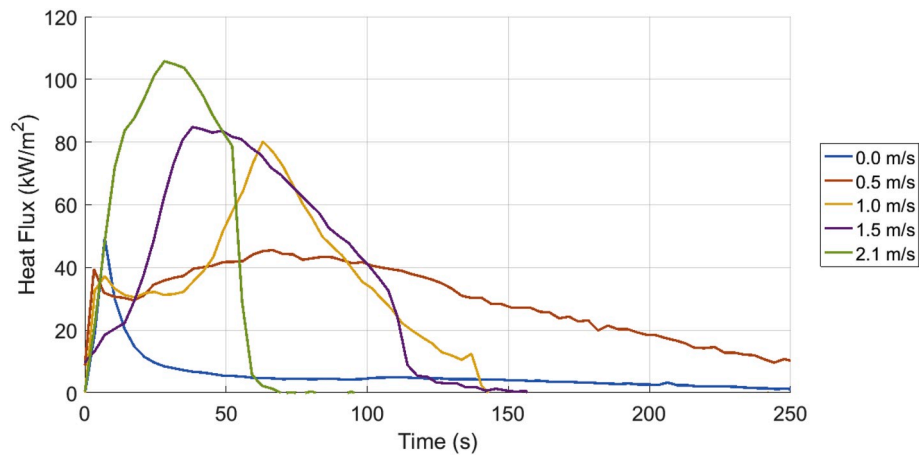


Fig. 11. Effect of wind speed on heat flux at the peak location with time for the cuboid $L = 38$ mm, one notch firebrand with the long side perpendicular to the wind.

Table 2

Summary of heat fluxes measured in this work at different resolutions.

Description	Wind (m/s)	Wind Orientation	Peak Heat Flux (kW/m ²)		
			High Resolution	Avg. Over Firebrand	12.5 × 12.5 mm Region Avg.
Cuboid –	None	N/A	49	17.3	13.9
6.4 mm ×	1.0	Parallel	69.5	16	11.6
6.4 mm,	1.0	Perpendicular	79.6	15.6	17.4
38 mm					
long					
Cuboid –	None	N/A	49.3	19.7	11.5
6.4 mm ×	1.0	Parallel	71.9	16.8	12.9
6.4 mm,	0.5	Perpendicular	45.5	13.7	16.5
38 mm	1.0	Perpendicular	80.2	19.4	23.4
long	1.5	Perpendicular	84.8	15.6	22.7
One	2.1	Perpendicular	105.8	22.7	27
centered					
notch					
Cuboid –	None	N/A	41.7	18.3	17.4
6.4 mm ×	1.0	Parallel	73.7	19.4	16.8
6.4 mm,	1.0	Perpendicular	93.1	17.7	16.6
38 mm					
long					
Two					
centered					
notches					
Cuboid –	None	N/A	46.1	19.1	18.7
6.4 mm ×	1.0	Parallel	71.1	19.8	15.4
6.4 mm,	1.0	Perpendicular	61.8	16.2	14.9
38 mm					
long					
End					
notches					
Cylinder	None	N/A	33.1	13.8	7.4
– 6.4 mm	1.0	Parallel	51.4	15.4	9.7
diameter,	1.0	Perpendicular	28.1	15.8	7.9
38 mm					
long					
Cuboid –	None	N/A	94.5	27.1	20.8
6.4 mm ×	1.0	Parallel	85.5	23.5	16.8
6.4 mm,	1.0	Perpendicular	88.4	26.1	20.8
25 mm					
long					

firebrand trends were different due to flow around the firebrand.

Spatial distributions in the fire brand heat flux levels are provided in Fig. 9 for the different types of firebrands at the time of the peak heat flux level. For this case, the firebrands with notches had higher heat fluxes in the locations with the notches compared with the direct contact with the plate. This is likely due to the wind blowing through these

notches, elevating the surface temperatures and increasing the radiation from the firebrand to the surface at these locations. There are also higher heat fluxes at the ends of the firebrand, which is attributed to more char oxidation on the ends where there is more surface area.

3.4. Firebrand temperature

The firebrand temperature distribution at the time of the peak temperature is provided in Fig. 10. The peak temperatures range from 300 to 775 °C for cylindrical firebrands to 800–950 °C for the cuboid firebrands. Highest temperatures were measured at the ends where there is more surface area for char oxidation.

3.5. Wind speed effects

The effects of wind speed on firebrand heat flux levels are provided in Fig. 11 for a cuboid $L = 38$ mm with a one notch in the center and wind perpendicular to the long side of the firebrand. As expected from previous work, increasing the wind speed causes an increase in heat flux level from 40 to 50 kW/m² with low wind speeds (up to 0.5 m/s) to 80–105 kW/m² for wind speeds of 1.0–2.0 m/s. In addition, the higher wind speeds caused the firebrands to be consumed faster resulting in intense but shorter duration exposures.

4. Discussion

A summary of the peak heat fluxes measured for the different firebrands in this study is provided in Table 2. In this table, the heat fluxes are provided at three different resolutions: high resolution, average over firebrand projected area on the surface, and average over a 12.5 mm × 12.5 mm region.

The firebrand average heat flux was calculated to allow for comparison with heat fluxes predicted using an energy balance on the firebrand [11]. The energy balance prediction of heat flux from a cylindrical firebrand (10 mm in diameter, 75 mm long) was 23 kW/m² with a 1.3 m/s wind [11]. This is approximately 32% higher than the cylinder tested in this work but within 22% of the cuboids. The deviations between the two studies are attributed to the differences in firebrand temperatures.

The 12.5 mm × 12.5 mm average was calculated to compare with measurements using a 12.5 mm diameter heat flux gauge by Hakes et al. [12]. They measured heat fluxes ranging from 7 to 25 kW/m² for single cylindrical brands 6.4–12.7 mm in diameter and 25 mm long with no wind. This is consistent with the range of 12.5 mm × 12.5 mm average heat flux levels measured in this study shown in Table 2.

The higher resolution heat fluxes are a factor of 2–6 times higher

than the spatially averaged heat fluxes. Some of these heat fluxes are quite localized and the spatial resolution that drives ignition will need to be determined with future experiments of firebrands on combustible materials. Despite this, the technique presented in this paper is able to capture these spatial variations allowing for appropriate averaging to assess the ignition potential of single firebrands and firebrand piles. In addition, the spatial heat flux distributions produced using these measurements also captures the location of the peak heat fluxes which can be uncertain based on the firebrand geometry, contact, and orientation with wind direction.

5. Conclusions

An experimental study was performed to measure the localized heat fluxes produced by different types of single firebrands onto a horizontal surface under different wind conditions. An inverse heat transfer method using a series of IR thermographs of a stainless steel plate provided spatial heat flux distributions with a 0.4 mm resolution. With the higher resolution, peak heat fluxes were measured to be 30–105 kW/m², which is 2–6 times higher than expected based on lower spatial resolutions and values reported in the literature. Firebrand geometry, wind speed and wind orientation relative to the firebrand all affected the peak heat flux produced by the firebrand and the exposure duration. Cuboid shaped firebrands were measured to produce higher heat fluxes than cylindrical shaped firebrands. Notches on the cuboid firebrands varying the contact between the firebrand and surface caused higher heat fluxes due to more radiation from the oxidizing surfaces in the notch. The leading edge of the firebrand oriented parallel to the wind had the highest heat flux levels. Firebrand experiments on combustible surfaces are needed to determine the appropriate heat flux resolution to correlate with the ignition of the combustible.

Declaration of competing interest

The authors declare the following financial interests/personal relationships which may be considered as potential competing interests: Brian Lattimer has an ownership/equity interest in Jensen Hughes. This is stated in the acknowledgements of the paper.

Acknowledgements

The project was funded through NIST Grant No. 70NANB19H052.

References

- [1] S.E. Caton, R.S.P. Hakes, D.J. Gorham, A. Zhou, M.J. Gollner, Review of pathways for building fire spread in the wildland urban interface Part I: exposure conditions, *Fire Technol.* 53 (2) (2017) 429–473.
- [2] R.S.P. Hakes, S.E. Caton, D.J. Gorham, M.J. Gollner, A review of pathways for building fire spread in the wildland urban interface Part II: response of components and systems and mitigation strategies in the United States, *Fire Technol.* 53 (2) (2017) 475–515.
- [3] E. Koo, P.J. Pagni, D.R. Weise, J.P. Woycheese, Firebrands and spotting ignition in large-scale fires, *Int. J. Wildland Fire* 19 (7) (2010) 818–843.
- [4] S.L. Manzello, Enabling the investigation of structure vulnerabilities to wind-Driven firebrand showers in wildland-Urban Interface (WUI) fires, *Fire Saf. Sci.* 11 (2014) 83–96, 11.
- [5] V.P. Dowling, Ignition of timber bridges in bushfires, *Fire Saf. J.* 22 (2) (1994) 145–168.
- [6] P. Ellis, The Aerodynamic and Combustion Characteristics of Eucalypt Bark - A Firebrand Study, Dissertation, Aust. Natl. Univ. Dep. For., 2000, p. 205.
- [7] T.J. Ohlemiller, Smoldering combustion propagation on solid wood, *Fire Saf. Sci.* 3 (2006) 565–574.
- [8] S.L. Manzello, T.G. Cleary, J.R. Shields, A. Maranghides, W. Mell, J.C. Yang, Experimental investigation of firebrands: generation and ignition of fuel beds, *Fire Saf. J.* 43 (3) (2008) 226–233.
- [9] S.L. Manzello, T.G. Cleary, J.R. Shields, J.C. Yang, On the ignition of fuel beds by firebrands, *Fire Mater.* 30 (1) (2006) 77–87.
- [10] A. Warey, Influence of thermal contact on heat transfer from glowing firebrands, *Case Stud. Therm. Eng.* 12 (May) (2018) 301–311.
- [11] S.L. Manzello, S.H. Park, T.G. Cleary, Investigation on the ability of glowing firebrands deposited within crevices to ignite common building materials, *Fire Saf. J.* 44 (6) (2009) 894–900.
- [12] R.S.P. Hakes, H. Salehizadeh, M.J. Weston-dawkes, M.J. Gollner, Thermal characterization of firebrand piles, *Fire Saf. J.* 104 (2019) 34–42. June 2018.
- [13] S.L. Manzello, S. Suzuki, Exposing decking assemblies to continuous wind-driven firebrand showers, *Fire Saf. Sci.* 11 (2014) 1339–1352.
- [14] S.S. Wessies, M.K. Chang, K.C. Marr, O.A. Ezekoye, Experimental and analytical characterization of firebrand ignition of home insulation materials, *Fire Technol.* 55 (3) (2019) 1027–1056.
- [15] J.L. Urban, A.C. Fernandez-pello, M. Vicariotto, D. Dunn-Rankin, Temperature measurement of glowing embers with color pyrometry, *Fire Technol.* 55 (3) (2019) 1013–1026.
- [16] Y.M. Abul-huda, Development of a spatially resolved optical technique for measuring heat flux and thermal footprint of firebrand piles, *NIST Tech. Note* 2052 28 (2019).
- [17] J. Hodges, C. Rippe, S.W. Case, B.Y. Lattimer, Predicting the structural response of a compartment fire using full-field heat transfer measurements, *Fire Saf. J.* 91 (March) (2017) 471–479.
- [18] C.M. Rippe, B.Y. Lattimer, Full-field surface heat flux measurement using non-intrusive infrared thermography, *Fire Saf. J.* 78 (2015) 238–250.
- [19] N. Cholewa, P.T. Summers, S. Feih, A.P. Mouritz, B.Y. Lattimer, S.W. Case, A technique for coupled thermomechanical response measurement using infrared thermography and digital image correlation (TDIC), *Exp. Mech.* 56 (2016) 145–164.
- [20] R.J. Goldstein, E.M. Sparrow, D.C. Jones, Natural convection mass transfer adjacent to horizontal plates, *Int. J. Heat Mass Tran.* 16 (5) (1973) 1025–1035.
- [21] J.R. Lloyd, W.R. Moran, Natural convection adjacent to horizontal surface of various planforms, *J. Heat Tran.* 96 (4) (1974) 443–447.
- [22] F.P. Incropera, D.P. Dewitt, T.L. Bergman, A.S. Lavine, *Fundamentals of Heat and Mass Transfer*, sixth ed., Wiley, 2007.